Journal of Biomechanics 93 (2019) 194–203

Contents lists available at ScienceDirect

Journal of Biomechanics

journal homepage: www.elsevier.com/locate/jbiomech
www.JBiomech.com

Development and validation of subject-specific pediatric multibody knee kinematic models with ligamentous constraints

Martina Barzan [a,*], Luca Modenese [a,b], Christopher P. Carty [a,c], Sheanna Maine [d], Christopher A. Stockton [e], Nicola Sancisi [f], Andrew Lewis [g], James Grant [g], David G. Lloyd [a], Simao Brito da Luz [a]

[a] Gold Coast Centre for Orthopedic Research, Engineering and Education, Menzies Health Institute Queensland and School of Allied Health Sciences, Griffith University, Gold Coast, Australia
[b] Department of Civil and Environmental Engineering, Imperial College London, United Kingdom
[c] Queensland Children's Motion Analysis Service, Queensland Pediatric Rehabilitation Service, Children's Health Queensland Hospital and Health Service, Brisbane, Australia
[d] Department of Orthopedics, Children's Health Queensland Hospital and Health Service, Brisbane, Australia
[e] Department of Medical Imaging and Nuclear Medicine, Children's Health Queensland, Lady Cilento Children's Hospital, Brisbane, Australia
[f] Department of Industrial Engineering, Università degli Studi di Bologna, Italy
[g] School of Information and Communication Technology, Griffith University, Nathan, Australia

ARTICLE INFO

Article history:
Accepted 2 July 2019

Keywords:
Secondary knee joint kinematics
Ligament length
Parallel mechanism
Subject-specific
Pediatric

ABSTRACT

Computational knee models that replicate the joint motion are important tools to discern difficult-to-measure functional joint biomechanics. Numerous knee kinematic models of different complexity, with either generic or subject-specific anatomy, have been presented and used to predict three-dimensional tibiofemoral (TFJ) and patellofemoral (PFJ) joint kinematics of cadavers or healthy adults, but not pediatric populations.

The aims of this study were: (i) to develop subject-specific TFJ and PFJ kinematic models, with TFJ models having either rigid or extensible ligament constraints, for eight healthy pediatric participants and (ii) to validate the estimated joint and ligament kinematics against *in vivo* kinematics measured from magnetic resonance imaging (MRI) at four TFJ flexion angles.

Three different TFJ models were created from MRIs and used to solve the TFJ kinematics: (i) 5-rigid-link parallel mechanism with rigid surface contact and isometric anterior cruciate (ACL), posterior cruciate (PCL) and medial collateral (MCL) ligaments (ΔL_{null}), (ii) 6-link parallel mechanism with minimized ACL, PCL, MCL and lateral collateral ligament (LCL) length changes (ΔL_{min}) and (iii) 6-link parallel mechanism with prescribed ACL, PCL, MCL and LCL length variations (ΔL_{match}). Each model's geometrical parameters were optimized using a Multiple Objective Particle Swarm algorithm.

When compared to MRI-measured data, ΔL_{null} and ΔL_{match} performed the best, with average root mean square errors below 6.93° and 4.23 mm for TFJ and PFJ angles and displacements, respectively, and below 2.01 mm for ligament lengths (<4.32% ligament strain). Therefore, within these error ranges, ΔL_{null} and ΔL_{match} can be used to estimate three-dimensional pediatric TFJ, PFJ and ligament kinematics and can be incorporated into lower-limb models to estimate joint kinematics and kinetics during dynamic tasks.

1. Introduction

Numerous knee joint kinematic models have been developed and vary from simple mechanisms to more complex and anatomically correct representations of the joint. Previous studies (Andersen et al., 2010; Stagni et al., 2009) demonstrated that the knee represented as hinge or spherical joint cannot accurately estimate *in vivo* secondary knee kinematics (i.e., ab/adduction, internal/external rotation, and anterior/posterior, proximal/distal, medio/lateral translations), especially joint translations. However, more realistic five-rigid-link parallel (i.e., closed-loop) mechanisms have been proposed for the tibiofemoral joint (TFJ), consisting of two rigid tibial and femoral contacts and isometric anterior cruciate (ACL), posterior cruciate (PCL) and medial collateral (MCL) ligaments (Feikes et al., 2003; Ottoboni et al., 2010; Parenti-Castelli and Di Gregorio, 2000; Sancisi and Parenti-Castelli, 2011a; Wilson et al., 1998), and patellofemoral joint (PFJ), represented as a hinge joint between the femur

* Corresponding author at: Gold Coast Centre for Orthopedic Research, Engineering and Education, Menzies Health Institute Queensland and School of Allied Health Sciences, Griffith University, Gold Coast campus, Parklands Drive, Southport, QLD 4222, Australia.
E-mail address: martina.barzan@griffithuni.edu.au (M. Barzan).

https://doi.org/10.1016/j.jbiomech.2019.07.001
0021-9290/

and the patella and an isometric patellar tendon (Sancisi and Parenti-Castelli, 2011a). These mechanisms estimated *in vitro* passive six motion components (three rotations, three translations) of each joint, with mean errors below 2.4° for rotations and 1.9 mm for translations (Sancisi and Parenti-Castelli, 2011b), while allowing for computational convenience and not needing to resort to continuum models (Adouni et al., 2012; Halonen et al., 2017; Kiapour et al., 2014; Mootanah et al., 2014). Furthermore, parallel mechanisms have been generated from magnetic resonance imaging (MRI) in healthy adults (Brito da Luz et al., 2017), and extended to perform dynamic analyses (Moissenet et al., 2014).

More complex parallel TFJ mechanisms have also been proposed. Gasparutto et al. (2012) added the lateral collateral ligament (LCL) to the previously described five-rigid-link model and allowed for minimal ligament deformation during passive and loaded gait conditions. These models better predicted internal/external TFJ rotation during running compared to isometric ligament models (Gasparutto et al., 2015). Moreover, when compared to simple and/or generic TFJ models, personalized parallel TFJ mechanisms with minimally deformable ligaments can better estimate TFJ ab/adduction, internal/external rotation and anterior/posterior translation during squatting in healthy and osteoarthritic adults (Clément et al., 2015). Additionally, Moissenet et al. (2014) included a passive PFJ mechanism in their musculoskeletal model to perform gait analysis. However, these TFJ and PFJ models have only been implemented in adult populations, and seldom validated (Clément et al., 2015; Gasparutto et al., 2015). Therefore, it is unclear whether adding minimally deformable ligaments to these models can help capture anatomical characteristics typical of the pediatric population, including high inter-subject anatomical variability and increased TFJ laxity that diminishes with increasing age (Flynn et al., 2000; Hinton et al., 2008).

For validation purposes, estimated subject-specific knee joint kinematics are generally compared against *in vivo* knee kinematics measured using imaging techniques, such as fluoroscopy (Lu et al., 2008; Marra et al., 2015) or biplanar radiography (Clément et al., 2015), or intracortical pins (Benoit et al., 2006; Bonci et al., 2014; Reinschmidt et al., 1997). However, radiation exposure or invasive procedures limit the use of these methods, especially in pediatric populations. Alternatively, MRI is a safe technology for validation of knee mechanisms in children. To date, no studies have developed and validated subject-specific TFJ and PFJ mechanisms for children using MRI.

Therefore, this study first aimed to use MRI to generate three subject-specific TFJ models, with varying complexity (i.e., have different ligamentous constraints), each combined with a subject-specific PFJ model to estimate three-dimensional TFJ and PFJ kinematics in a healthy pediatric population. The second aim was to validate the kinematic results from the three different TFJ models against knee kinematics and ligament lengths measured from MRI scans collected at four unloaded knee flexion angles. We hypothesized that, compared to the simplest model with three rigid knee ligaments, the two models with increased complexity, obtained by adding an extra knee ligament and by allowing for minimal or prescribed elongation (Belvedere et al., 2012; Bergamini et al., 2011; Blankevoort et al., 1991) of the ligaments, would provide better estimates of MRI-measured joint and ligament kinematics across the four knee flexion angles.

2. Methods

2.1. Participants

Eight healthy children and adolescents (4 males and 4 females, mean ± SD: age 14.0 ± 2.6 years, mass 51.1 ± 10.5 kg, height 1.64 ± 0.11 m) were recruited. Study approval was obtained from the Children's Health Queensland Hospital and Health Services human research ethics committee (HREC/13/QRCH/197) and participants' guardians provided written informed consent.

2.2. Medical image acquisition and processing

Three sets of MRIs were collected at the Queensland Children's Hospital (Brisbane, Australia) from each participant. First, a full lower-body scan (1.5 T, SIEMENS MAGNETOM Avanto_fit syngo MR VE11B, Germany), including the pelvis and lower limb bones (3D PD SPACE, slice thickness: 1.0 mm, voxel size: $0.83 \times 0.83 \times 1.0\ mm^3$), was performed with the participant in a supine position. Second, a regional unloaded scan (3 T, SIEMENS MAGNETOM Skyra, Germany) of the participant's right knee (3D SPC T2, slice thickness: 0.53 mm, voxel size: $0.53 \times 0.53 \times 0.53\ mm^3$) was performed with the knee at ~0° TFJ flexion using a dedicated knee coil. Third, three additional dedicated right knee scans were acquired under small gravitational loads at ~7°, 15° and 25° of TFJ flexion by using a flexible array coil wrapped around the knee.

Three-dimensional lower limb bones, knee ligamentous and cartilaginous structures were segmented in Mimics Research 20.0 (Materialise, Belgium) from each participant's scans. Segmented bones included the femur, patella, tibia and fibula, while ligaments included the ACL, PCL, MCL and LCL (Fig. 1) and patellar tendon. Three-dimensional full-length bones were registered with the three-dimensional knee reconstructions through an iterative closest point algorithm (Besl and McKay, 1992) in 3-matic (Materialise, Belgium) to obtain a comprehensive representation of the participant's anatomy at each considered knee angle.

2.3. Subject-specific TFJ and PFJ kinematic models

A baseline TFJ model was implemented as a five-link parallel mechanism including two sphere-on-sphere contacts (representing the medial and lateral contacts between the femoral condyles and the tibial plateaus) and three ligaments (ACL, PCL and MCL) (Brito da Luz et al., 2017; Sancisi and Parenti-Castelli, 2011a) (Fig. 1b). The two articular contacts were considered rigid, with no penetration or separation permitted. The geometry of the contact surfaces (i.e., sphere centers and radii) was obtained from MRI by approximating the femoral condyles and tibial plateaus by best-fitting spheres (Matlab R2014b, MathWorks). The geometry of the ligaments (i.e., ligament lengths, attachment points) was derived from the MRI at ~0° TFJ flexion by computing the centroids of the segmented ligament attachment regions on the corresponding bones. The TFJ baseline model was then extended by adding the LCL (i.e., six-link), whose geometry was defined with the same procedure used for the other ligaments.

Different TFJ models were created with three different ligament models. The *first* was a five-rigid-link TFJ model where the ACL, PCL and MCL were considered isometric (ΔL_{null}) over the TFJ flexion range of motion (ROM). The *second* was a six-link TFJ model with minimal ACL, PCL, MCL and LCL (ΔL_{min}) length variations over the TFJ flexion ROM. The *third* was a six-link TFJ model where the ACL, PCL, MCL and LCL length variations tracked the pattern of published experimental ligament length variations (ΔL_{match}) (Belvedere et al., 2012; Bergamini et al., 2011; Blankevoort et al., 1991) over the TFJ flexion ROM.

The PFJ was modelled as a hinge joint, where the patella was constrained to rotate about and at a constant distance from an axis while maintaining constant patellar tendon length. The axis was defined by the center of two spheres fitted to the medial and lateral patellofemoral articular surfaces (Brito da Luz et al., 2017; Sancisi and Parenti-Castelli, 2011a). Finally, femur, tibia and patella

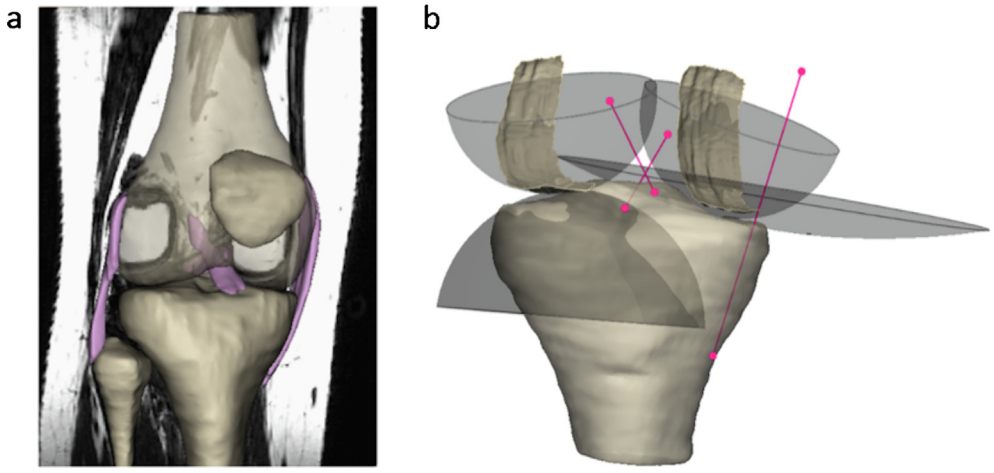

Fig. 1. Example of bone and TFJ ligament segmentation from the regional MRI scan (a). Baseline model of the TFJ (ΔL_{null}) (b): the spherical surfaces (grey) approximate the geometry of the femoral condyles and tibia plateaus, while the rigid links (fuchsia) represent the isometric fibers of ACL, PCL and MCL.

segment coordinate systems (SCSs) were defined (Belvedere et al., 2007; Cappozzo et al., 1995) using anatomical landmarks manually located onto the bone segmented surfaces (Table S1 supplementary material) to derive the relative poses of the bones as a result of the model. Since the PFJ hinge axis was not aligned to the femur medio-lateral axis, the single rotation about the hinge axis was decomposed into coupled rotations about all reference axes.

2.4. Tuning of each subject-specific TFJ model

After each subject-specific TFJ and PFJ model was created, tuning (i.e., optimization) of the model's geometrical parameters (initially measured off the MRIs) was undertaken to ensure that the corresponding joint mechanism could be solved without singularities (Brito da Luz et al., 2017). For the three different TFJ ligament models, we employed different optimization approaches, each consisting of an *outer* and *inner* loop. The *outer* loop optimized each participant's MRI-measured geometrical parameters (i.e., sphere centers and ligament attachment points), while the *inner* loop solved the TFJ and PFJ mechanisms. In the *outer* loop, the three-dimensional coordinates of the sphere centers were adjusted within a range that was proportional to the size of the spheres (Tables S2–S5 supplementary material) and that allowed the joint mechanisms to solve for each participant (20 mm for the TFJ models, 5 mm for the PFJ model). The radii of these spheres were also updated by minimizing the summed least square residuals between fitted spheres and MRI-segmented cartilages and ensuring that the residuals were <5% of the optimized radii. Finally, the optimized attachment points of the ligaments were maintained within their respective bone attachment regions.

Depending on the TFJ ligament model, the *outer* loop optimized for four different objective functions (see Eqs. (1)–(4) and Table 1 for full definition of terms). Eq. (1) best matched the pattern between estimated and published experimental TFJ and PFJ kinematics, ensuring TFJ and PFJ motion consistent with those measurements (Brito da Luz et al., 2017). Eq. (2) minimized the difference between MRI-measured and optimized geometrical parameters, to ensure that they were close, thereby well representing each participant's anatomy (Brito da Luz et al., 2017). Eq. (3) minimized the difference between optimized and published pediatric TFJ ab/adduction and internal/external rotation ROMs, if the optimized ROMs were larger than the published ROMs. This cost function guaranteed that the estimated TFJ ab/adduction and internal/external rotation were within reasonable ROM for healthy pediatric individuals. However, the lack of published pediatric data describing TFJ translations and PFJ kinematics impeded constraint of other ROMs. Finally, Eq. (4) best matched the pattern between estimated and published experimental ligament length variations, ensuring physiological length variation for the four ligaments. Eqs. (1)–(3) were used for all ligament models, while Eq. (4) only for ΔL_{min} as this condition was already achieved in the *inner loop* for ΔL_{match}.

Table 1
Description of terms in Eqs. (1)–(4).

Equation	Symbol	Description
1	$\rho_{joint,i}$	Pearson's correlation between ith estimated and published TFJ (Ottoboni et al., 2010; Sancisi and Parenti-Castelli, 2011a, 2011b) and PFJ (Anglin et al., 2008; Sancisi and Parenti-Castelli, 2011a, 2011b) N_{DOFs} kinematics
	N_{DOFs}	total number of TFJ (N_{DOFs} = 5) and PFJ (N_{DOFs} = 6) dependent degrees of freedom
2	$g_{m,k}$	kth measured geometrical parameter
	$g_{o,k}$	kth optimized geometrical parameter
	N_{geom}	total number of TFJ geometrical parameters (i.e. center of the two spheres fitted to the tibial plateaus and ligament attachment points) used in ΔL_{null} (N_{geom} = 24), ΔL_{min} and ΔL_{match} (N_{geom} = 30)
3	$ROM_{o,n}$	nth optimized ROM
	$ROM_{m,n}$	nth measured ROM during gait in children (Leardini et al., 2007)
	$N_{DOFs\ bound}$	total number of bounded TFJ ROM degrees of freedom ($N_{DOFs\ bound}$ = 2 in this case, i.e. TFJ ab/adduction and internal/external rotation)
4	$\rho_{ligament,l}$	Pearson's correlation between the lth estimated and published (Belvedere et al., 2012; Bergamini et al., 2011; Blankevoort et al., 1991) ligament kinematics
	N_{lig}	total number of ligaments used in ΔL_{min} (N_{lig} = 4)

$$J_1 = \left(1 - \rho_{joint,i}\right)^2 \qquad i = 1, \cdots, N_{DoF} \tag{1}$$

$$J_2 = \left(g_{m,k} - g_{o,k}\right)^2 \qquad k = 1, \cdots, N_{geom} \tag{2}$$

$$J_3 = \begin{cases} 0 & \text{if } ROM_{o,n} \le ROM_{m,n} \\ mean\left[(ROM_{o,n} - ROM_{m,n})^2\right] & \text{if } ROM_{o,n} > ROM_{m,n} \end{cases} \quad n = 1, \cdots, NDoFs \text{ bound} \tag{3}$$

$$J_4 = \left(1 - \rho_{ligament,l}\right)^2 \qquad l = 1, \cdots, N_{lig} \tag{4}$$

Multiple Objective Particle Swarm Optimization (MOPSO) (Coello et al., 2004) (Matlab) optimized the geometrical parameters to minimize the corresponding objective functions in the *outer* loop. MOPSO generated multiple solutions (Fig. S17 supplementary material) from which the following criteria were used to choose a unique solution (S):

$$S_{\Delta L_{null},\Delta L_{match}} = \begin{cases} min\ J_1 & \text{if } J_3 = 0 \\ min\ J_3 & \text{if } J_3 > 0 \end{cases} \tag{5}$$

$$S_{\Delta L_{min}} = \begin{cases} min[mean(J_1, J_4)] & \text{if } J_3 = 0 \\ min\ J_3 & \text{if } J_3 > 0 \end{cases} \tag{6}$$

Importantly, J_2 was never included in the choice of optimal solutions because the geometrical parameters were always within the limits of reasonable anatomical variability. To ensure this, the TFJ and PFJ sphere centers could deviate, on average, up to 3% and 18% of the radius of the spheres fitted to the corresponding MRI-segmented cartilage, and the ligament attachment points were within their attachment regions.

The *inner* loops for the TFJ and PFJ mechanisms used the set of geometrical parameters to solve the closure equations of the joint mechanisms for 1° increments of the TFJ flexion angle from 0° to 90°. The solved equations estimated the remaining TFJ rotations and translations while ensuring these were continuous, i.e. without singularities. Depending on the type of ligament model, the *inner* loop minimized the estimated ligament length changes for ΔL_{null} and ΔL_{min}, or the difference between estimated and published experimental ligament length change for ΔL_{match}. The joint mechanisms' closure equations were solved by using the *fsolve* function in Matlab, with a trust-region algorithm for ΔL_{null}, and a Levenberg-Marquardt method for ΔL_{min} and ΔL_{match}, since in these two models the number of closure equations exceeded the number of dependent degrees of freedom.

2.5. Data analysis and statistics

For validation, we determined the experimental poses of each participant's tibia and patella with respect to their femur from the MRIs at approximately 0°, 7°, 15° and 25° of TFJ flexion angle (Fig. 2). The anatomical landmarks identified in the MRI-reference 0° position, and used to create the initial SCSs, were identified on the corresponding registered bones at 7°, 15° and 25° positions (Fig. 2b–e). These landmarks were used to create the bones' SCSs and six-degrees-of-freedom kinematics at the four TFJ flexion angles. To ensure that the same fibers within each ligament were chosen, the transformation matrices aligning the SCSs in the MRI-reference pose to the SCSs in 7°, 15° and 25° flexion angles were computed and used to derive the ligaments' attachment points in all poses. For each model, ligaments' lengths were computed as Euclidean distance between the attachment points at all four different poses. The Root-Mean-Square Errors (RMSEs) between each participant's predicted and MRI-measured TFJ, PFJ and ligament kinematics were computed for each kinematic model and averaged across the four TFJ flexion angles. Ninety-five percent confidence intervals (CI) were also computed. A one-way repeated measures Analysis of Variance (ANOVA) with a priori contrasts was performed to determine differences in the average RMSE between each kinematic model at each TFJ and PFJ degree of freedom and ligament length ($\alpha = 0.05$).

Kinematic data were not normally distributed according to Shapiro-Wilk test results. Therefore, Statistical non-Parametric Mapping (SnPM) was used to assess the models' outputs (Pataky et al., 2015). Subsequently, the resulting average kinematic curves from the three models were compared to determine if significant differences existed between the curves at any TFJ flexion angle (Pataky et al., 2013). To-this-end, thirty-three nonparametric one-dimension two-tailed paired *t*-tests were conducted on the TFJ and PFJ kinematics, taking into consideration the dependency of all points of each TFJ flexion ROM ($\alpha = 0.05$) to calculate the critical

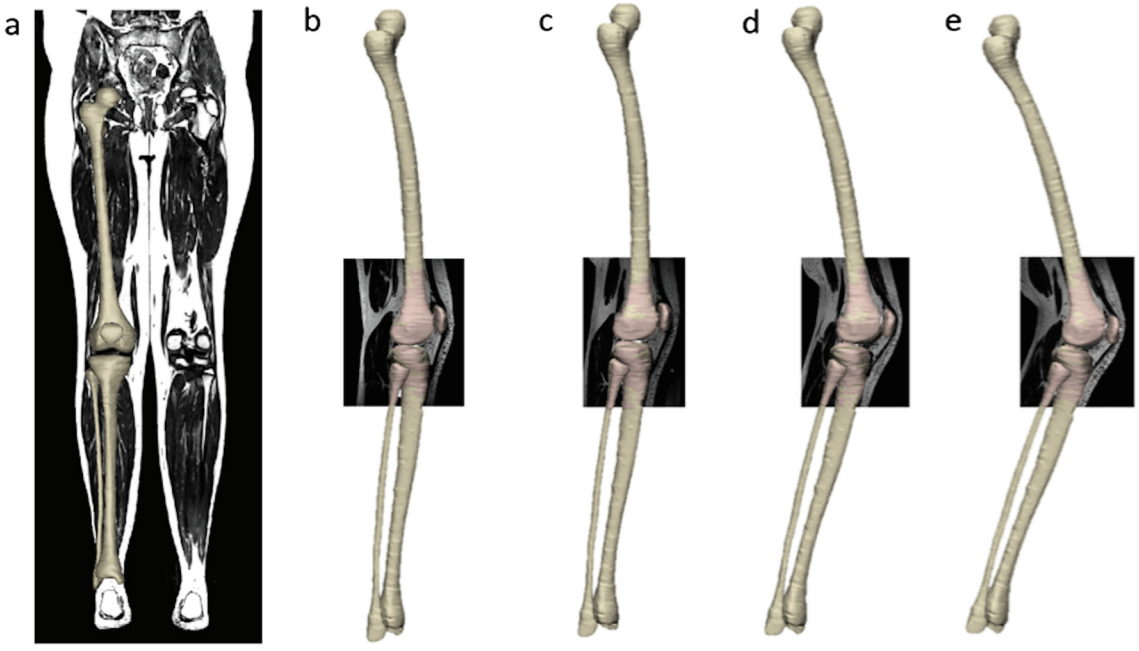

Fig. 2. Example of full-length bone segmentation from the full lower limb MRI scan (a). Example of bone segmentation from the regional MRI scans at approximately 0°(b), 7° (c), 15° (d) and 25° (e) of TFJ flexion and registration of these bones to the full-length bones (b, c, d, e).

threshold (t^*) (Penny et al., 2011). There was no correction for multiple hypothesis testing. All SnPM analyses were performed in Matlab using the open-source SPM1D code (version M.0.4.2, www.spm1d.org). Additionally, the similarity of the pattern of the TFJ and PFJ kinematic curves from the three models with those from published kinematics was examined using Pearson's correlation (ρ).

3. Results

Three different ligament models were produced and optimized for each participant and estimated their TFJ, PFJ and ligament kinematics (Figs. S9–S16 supplementary material). The optimization of the models' geometric parameters required ~5 h using a standard PC (Intel i5-4590S, 8 GB-RAM).

Generally, ΔL_{null} and ΔL_{match} exhibited lower average RMSEs for TFJ (rotations < 6.93°, translations < 1.91 mm) and PFJ (rotations < 3.90°, translations < 4.23 mm) kinematics than ΔL_{min} (TFJ rotations < 13.42°, TFJ translations < 3.15 mm, PFJ rotations < 5.76°, PFJ translations < 5.42 mm), suggesting that they better match the MRI-registered static poses (Fig. 3a and b). The average RMSEs for TFJ kinematics between ΔL_{null} and ΔL_{match} were not significantly different. Contrarily, average RMSEs in ΔL_{min} were significantly different to ΔL_{match} for TFJ ab/adduction (ΔL_{min}: 3.49° [2.73; 4.25 CI], ΔL_{match}: 1.81° [1.30; 2.32 CI]) and to ΔL_{null} for TFJ internal/external rotation (ΔL_{min}: 13.41° [9.42; 17.40 CI], ΔL_{null}: 5.41° [3.99; 6.83 CI]) (Fig. 3a). The RMSE magnitude in each TFJ and PFJ motion component was generally acceptable when assessed against the corresponding ROM (up to 90° TFJ flexion) for each participant (Tables S6 and S7 supplementary material). The average RMSEs for ligament length (between 0.60 mm and 2.01 mm) and strain (between 1.20% and 4.32%) were comparable between the three models (Fig. 3c and d), and remained close (<4.2%) to the MRI-registered ligament length at ~0° of TFJ flexion (Table S8 supplementary material).

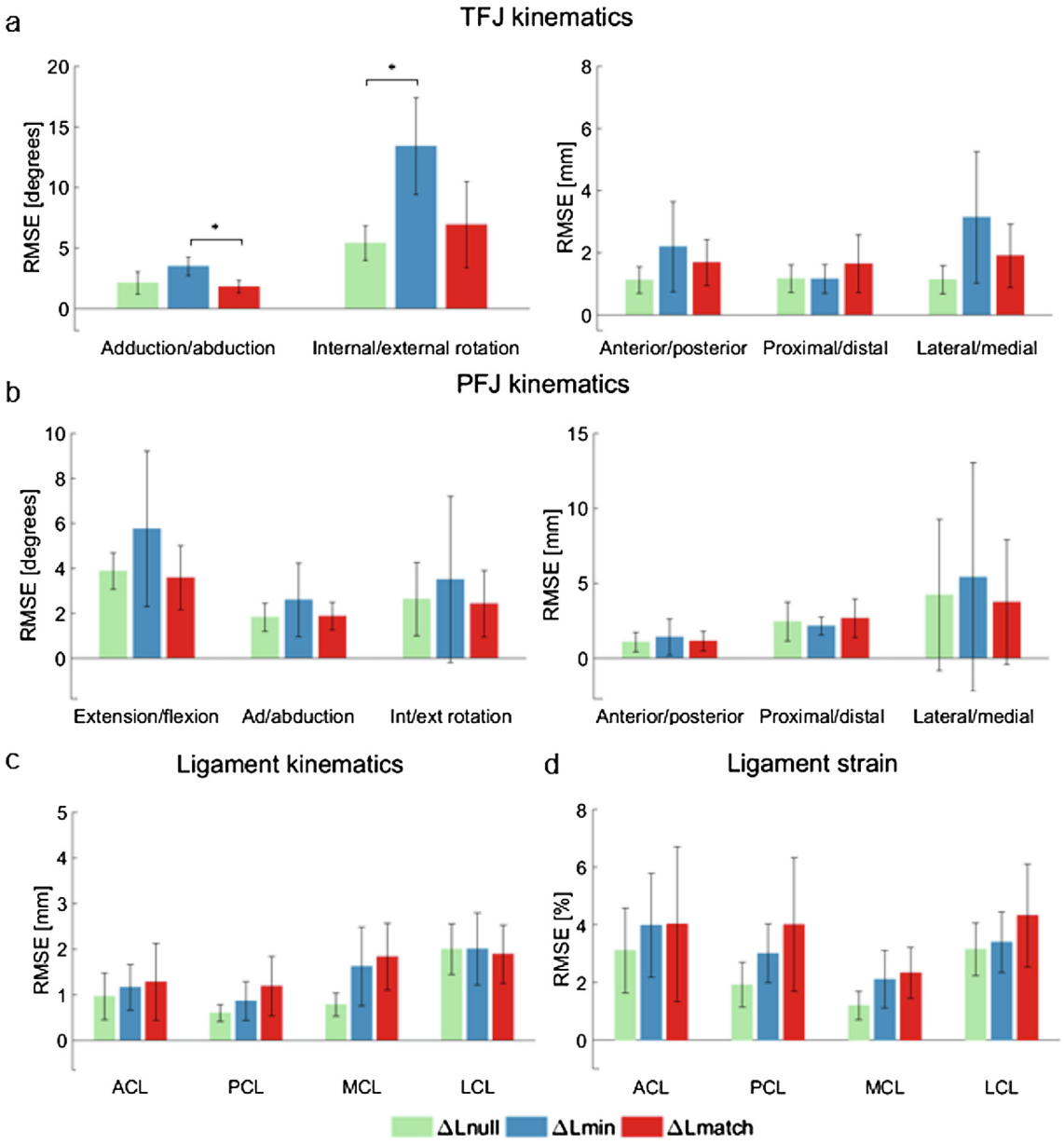

Fig. 3. Average RMSEs and 95% CI between estimated and MRI-measured TFJ kinematics (a), PFJ kinematics (b), ligament length (c) and strain (d) for each model. The length of the LCL in ΔL_{null} (c, d) was computed as the distance between the centroid of the attachment areas throughout the TFJ flexion ROM.

Paired *t*-tests showed differences in the modelled TFJ kinematics between the three models, while no differences were found in the PFJ kinematics between the three models (Figs. S1–S7 supplementary material). The mean TFJ ab/adduction for ΔL_{match} exhibited a more adducted pattern with respect to the other two models (Fig. 4), with significant differences at 14–69° of TFJ flexion with respect to ΔL_{null} and at 0–34° of TFJ flexion with respect to ΔL_{min}. Differences in TFJ ab/adduction were also found between ΔL_{null} and ΔL_{min} at 0–26° of TFJ flexion. Compared to the other two models, ΔL_{match} provided a smaller distal translation of the tibia with respect to the femur, with significant differences at 24–63° of TFJ flexion with respect to ΔL_{null} and at 56–69° of TFJ flexion with respect to ΔL_{min}.

The correlations between published and estimated TFJ and PFJ kinematics were very similar for the three models (Table 2). Specifically, for all three models, the resulting anterior/posterior and proximal/distal TFJ translations exhibited strong positive correlation with published kinematics ($\rho > 0.9$, $p < 0.01$), while

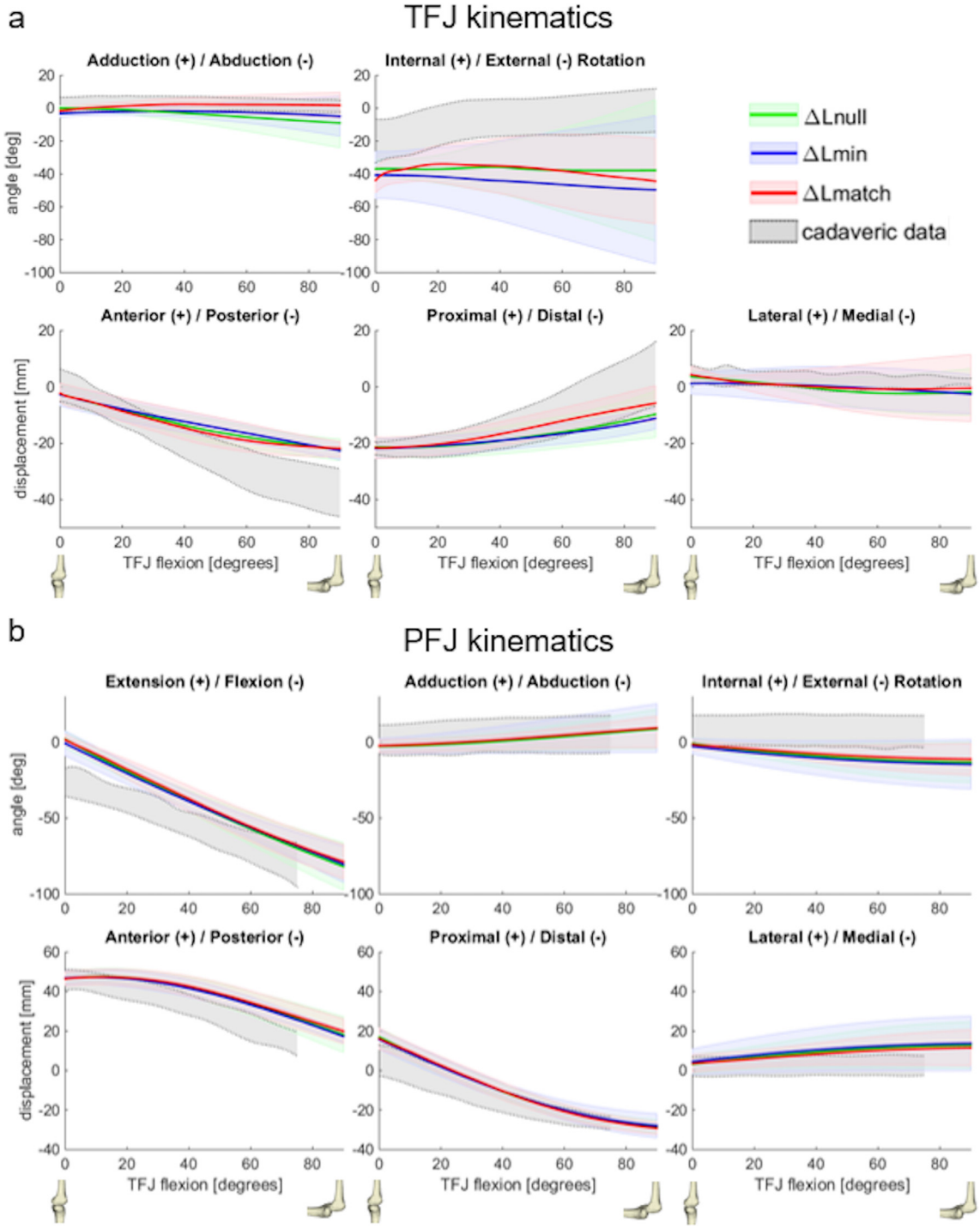

Fig. 4. Comparison between the average (a) TFJ and (b) PFJ kinematics as function of the TFJ flexion angle obtained from ΔL_{null} (green), ΔL_{min} (blue) and ΔL_{match} (red) models with those from published cadaveric data (grey) (TFJ: Ottoboni et al., 2010; Sancisi and Parenti-Castelli, 2011a, 2011b; PFJ: Anglin et al., 2008; Sancisi and Parenti-Castelli, 2011a, 2011b). Curves represent the average ± standard deviation across the eight participants. (For interpretation of the references to color in this figure legend, the reader is referred to the web version of this article.)

Table 2
Pearson's correlation coefficients across participants (average and standard deviation) between published and estimated TFJ and PFJ kinematics.

Joint	Model	Rotations			Translations		
		Flexion/extension	Ad/abduction	Internal/external	Anterior/posterior	Proximal/distal	Lateral/medial
TFJ							
	ΔL_{null}	–	0.10 (0.79)	0.01 (0.90)	0.99 (<0.01)	0.98 (0.02)	0.68 (0.59)
	ΔL_{min}	–	0.20 (0.79)	−0.23 (0.89)	0.99 (0.01)	0.97 (0.03)	0.51 (0.62)
	ΔL_{match}	–	0.22 (0.77)	0.11 (0.92)	0.98 (0.01)	0.97 (0.03)	0.48 (0.79)
PFJ							
	ΔL_{null}	>0.99 (<0.01)	0.93 (0.04)	0.69 (0.28)	>0.99 (<0.01)	>0.99 (<0.01)	0.93 (0.12)
	ΔL_{min}	>0.99 (<0.01)	0.93 (0.03)	0.69 (0.28)	>0.99 (<0.01)	>0.99 (<0.01)	0.93 (0.12)
	ΔL_{match}	>0.99 (<0.01)	0.92 (0.03)	0.70 (0.29)	>0.99 (<0.01)	>0.99 (<0.01)	0.93 (0.12)

model-estimated TFJ rotations showed very weak correlation with published kinematics ($-0.23 < \rho < 0.11$) and large variability. Conversely, PFJ kinematics had generally strong positive correlation with published PFJ translations and rotations, except for PFJ internal/external rotation ($\rho \geq 0.69$, $p < 0.01$).

Compared to published cadaveric data, the MRI-measured kinematic data generally overlapped with the published TFJ and PFJ kinematics ROMs, except for TFJ internal/external rotation (Fig. 5a) and PFJ extension/flexion (Fig. 5b). In fact, participants in this study exhibited a more externally rotated tibia and a more extended patella with respect to cadaveric kinematics. Moreover, compared to cadaveric ligament strain (Belvedere et al., 2012; Blankevoort et al., 1991), the MRI-measured data generally exhibited a slightly larger length variation with respect to the initial ligament length at 0° TFJ flexion (Fig. 6).

4. Discussion

In this study, we developed subject-specific pediatric TFJ and PFJ mechanisms from MRIs using three different ligament models, i.e. isometric (ΔL_{null}) and extensible ligaments (ΔL_{min}, ΔL_{match}). Each model was used to compute passive three-dimensional knee and ligament kinematics. We also validated the resulting kinematics from the three models against *in vivo* knee and ligament kinematics obtained from MRIs at four different TFJ flexion angles. When compared to MRI-measured data, ΔL_{null} and ΔL_{match} performed the best, with average RMSEs below 6.93° and 4.23 mm for TFJ and PFJ angles and displacements, respectively, and below 2.01 mm for ligament lengths (<4.23% ligament strain).

Contrary to our hypothesis, ΔL_{min} had the worst agreement with *in vivo* joint kinematics. It must be noted, however, that ligament lengths were minimized through parameter optimization at the stage of model creation, and did not rely on motion capture markers and their relative weights as in multibody optimization methods solved frame by frame (Gasparutto et al., 2015; Sancisi et al., 2017). Therefore, the ligament length minimization in the entire TFJ flexion ROM and the inclusion of an additional ligament (i.e., LCL), compared to Gasparutto et al. (2015), might have overconstrained ΔL_{min} and led to poor joint kinematics results. In comparison, ΔL_{null} and ΔL_{match} provided smaller average RMSEs, which were consistent with those obtained by Clément et al. (2015) (mean RMSEs < 5.2° and 4.3 mm) and Gasparutto et al. (2015) (mean RMSEs < 11.5° and 2.9 mm) using parallel TFJ mechanisms. Nevertheless, ΔL_{null} best predicted the MRI-measured length of ACL, PCL and MCL in the 0–25° TFJ flexion ROM, with RMSE magnitudes consistent with Sancisi et al. (2017), suggesting that these ligaments exhibit low length variation in the 0–25° TFJ flexion ROM (absolute average strain <8%, Fig. 6), as previously observed (Belvedere et al., 2012; Blankevoort et al., 1991). Therefore, ΔL_{match} may be the best model choice over a full range of knee flexion ROM.

Between the joint motion components, TFJ internal/external rotation exhibited the highest average RMSE (ΔL_{null}: 5.41°, ΔL_{min}: 13.41°, ΔL_{match}: 6.92°), in agreement with Clément et al. (2015) (average RMSE: 5.2 ± 3.8°), who compared active TFJ kinematics estimated by a TFJ parallel mechanism to those measured by biplanar radiography. However, when compared to published adult cadaveric data, both measured and modelled data of pediatric participants exhibited a more externally rotated tibia, together with a more extended patella. This might be a consequence of knee laxity in children (Baxter, 1988; Flynn et al., 2000; Hinton et al., 2008) in passive supine position, as confirmed by the larger MRI-measured ligament length variation, especially for the ligaments' fibers used for ΔL_{match} (Fig. 6).

The developed knee kinematic models rely on several assumptions based on experimental measurements. First, spheres were used to approximate the TFJ and PFJ articulating surfaces because they fitted the corresponding segmented surfaces with average residual values of 0.38 ± 0.17 mm (Table S9 supplementary material) and provided estimates of knee joint motion within 2.4° and 1.9 mm (Ottoboni et al., 2010; Sancisi and Parenti-Castelli, 2011b; Wilson and O'Connor, 1997) in the 0–90° of TFJ flexion ROM. Second, the articular TFJ and PFJ contacts were considered rigid, which is a reasonable assumption when external loads are not applied to the joints (i.e., passive motion) (Wilson and O'Connor, 1997). Third, as the passive forces applied by the muscle tendon units have been shown to have minimal influence on the passive TFJ kinematics (Ottoboni et al., 2010), they were not included in the models. Lastly, due to their geometrical similarity (i.e., congruence), articular PFJ surfaces were substituted by a hinge joint, which also replaced the function of the medial and lateral patellofemoral ligaments.

Within the context of the reported errors, the developed and validated pediatric knee models have potential clinical implications. First, these personalized models can characterize how the anatomy of the knee affects joint function in pediatric pathological conditions, including cerebral palsy, hypermobility syndrome or idiopathic lower limb malalignment. Second, the proposed models can be easily modified (i.e., with removal of constraints) to replicate unstable pediatric joint motion caused, for example, by ACL injury or lack of contact in the lateral TFJ compartment (e.g., severe achondroplasia). Lastly, these models can be used to predict, on an individual basis, how the joint function would vary after operative treatments, such as femoral derotation osteotomy or ACL reconstruction. However, extension of these models for clinical applications requires separate investigation and validation.

Why is predicting personalized pediatric knee and ligament kinematics using rigid-body models relevant for research? First, employing subject-specific (Clément et al., 2015) and more complex (compared to hinge) TFJ models has been shown to provide better estimates of secondary joint kinematics when using multibody kinematic optimization (Begon et al., 2018). Moreover, more accurate moment arm and muscle force estimates were achieved when using personalized TFJ kinematic models (Arnold et al., 2000; Navacchia et al., 2017). Second, the proposed rigid-body models, despite requiring initial tuning, provided quick estimates

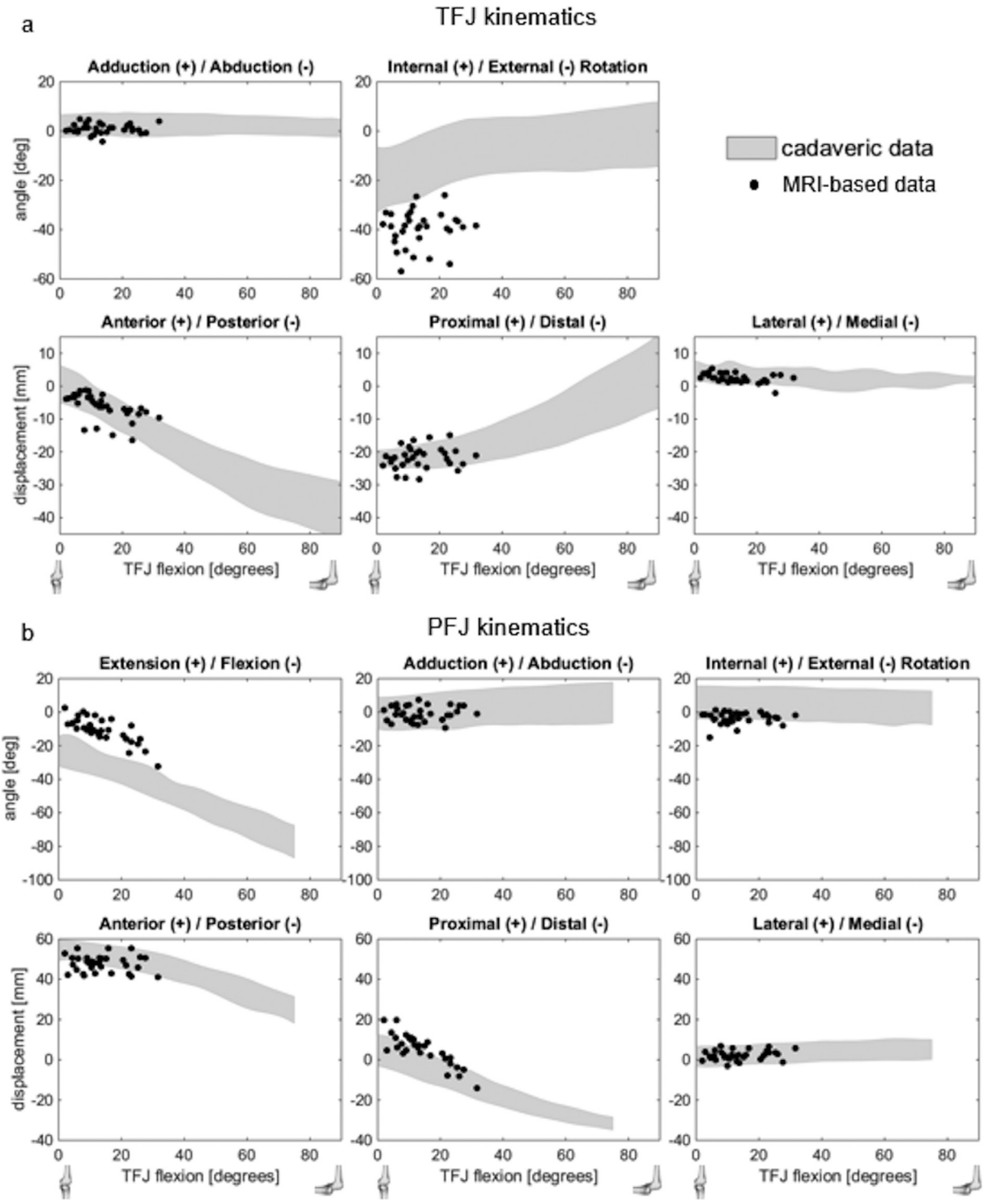

Fig. 5. Comparison between (a) TFJ and (b) PFJ kinematics from MRI-measured (black dots) and published cadaveric (grey) data (TFJ: Ottoboni et al., 2010; Sancisi and Parenti-Castelli, 2011; PFJ: Ottoboni et al., 2010; Sancisi and Parenti-Castelli, 2011) across the TFJ flexion ROM. The MRI-measured data include four poses for each participant.

of secondary knee kinematics compared to more complex and computationally expensive simulations (e.g., finite element) (Dhaher et al., 2010). Finally, morphological developmental changes at growth stresses the importance of child-specific knee kinematic models.

The proposed knee kinematic models and validation process have some limitations. Firstly, due to MRI bore size restraints, validation data were acquired in non-weight bearing static conditions at TFJ flexion angles <25°, which hindered validation at larger ROMs. Secondly, due to the lack of published pediatric knee and ligament kinematic data, the developed models were tuned using adult cadaveric data, presupposing comparable knee and ligament kinematics. This assumption seems reasonable for most degrees of freedom and ligaments, based on the agreement between MRI-measured and cadaveric data (Figs. 5 and 6). Future research could investigate the use of dynamic MRI to track the movement of soft

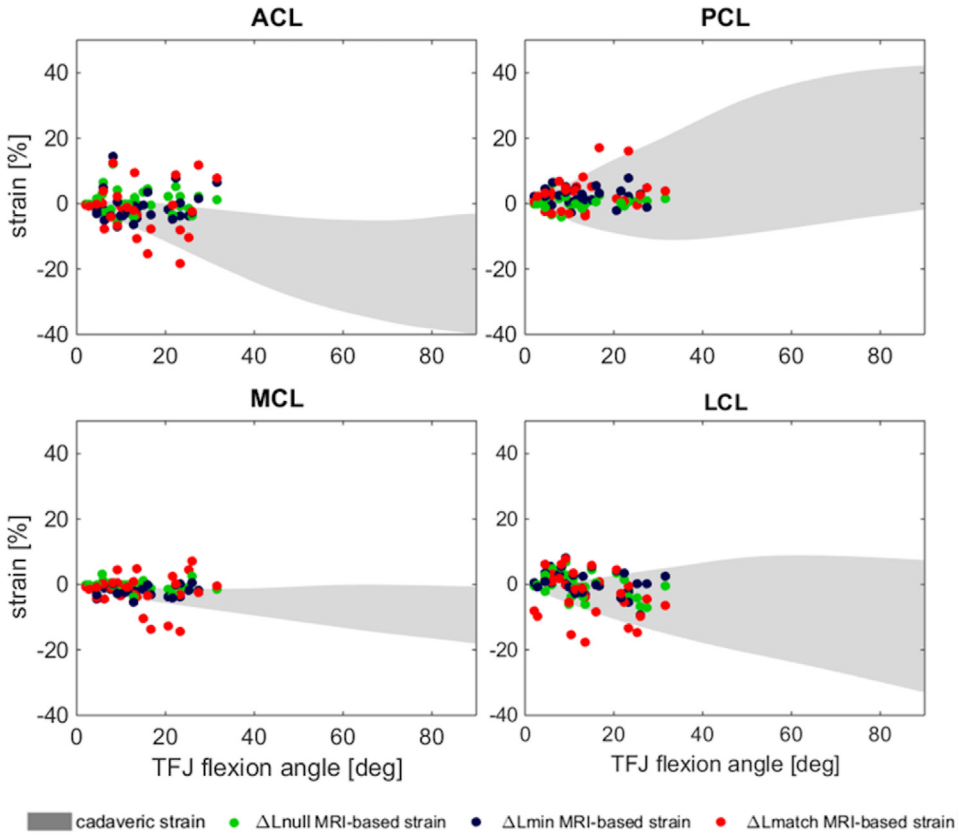

Fig. 6. Comparison of knee ligament strain (ACL, PCL, MCL and LCL) between published (Blankevoort et al., 1991; Belvedere et al., 2012) (grey) and MRI-measured data across the TFJ flexion ROM. The MRI-measured data (dots) include four poses for each participant and were calculated for ΔL_{null} (green), ΔL_{min} (blue) and ΔL_{match} (red). To calculate the strain, the initial length at 0° TFJ flexion of each ligament was derived from the respective model estimates. (For interpretation of the references to color in this figure legend, the reader is referred to the web version of this article.)

tissues and bones under loading conditions across TFJ flexion ROM (Macri et al., 2018), which would expand the model validation to larger TFJ flexion ROM and extend the applications of the model to task such as running and jumping.

In conclusion, this paper presented a methodology to create subject-specific TFJ and PFJ rigid body models with different ligamentous constraints from MRIs and applied it to a group of healthy children and adolescents. When compared to MRI-measured data, ΔL_{null} and ΔL_{match} performed the best (i.e., lowest RMSEs on average) and yielded similar results. Therefore, future model users could opt for ΔL_{null} to accurately estimate passive pediatric knee kinematics, or for ΔL_{match} to additionally well estimate ligament elongations. This work represents a step towards the creation of a fully subject-specific rigid-body model of the knee joint in pediatric populations, based on personalized geometries and anatomical structures. The importance of this development relies on the possibility of personalizing the joint kinematics and, therefore, improving all the dependent quantities of interest for musculoskeletal modelling such as muscle moment arms, articular contact points and ligament kinematics.

Declaration of Competing Interest

The authors declare that they do not have any financial or personal relationships with other people or organizations that could have inappropriately influenced this study.

Acknowledgements

L. Modenese was funded by an Imperial College Research Fellowship granted by Imperial College London, while C.P. Carty was funded by an Advance Queensland Research Fellowship granted by the Queensland Government.

Appendix A. Supplementary material

Supplementary data to this article can be found online at https://doi.org/10.1016/j.jbiomech.2019.07.001.

References

Adouni, M., Shirazi-Adl, A., Shirazi, R., 2012. Computational biodynamics of human knee joint in gait: from muscle forces to cartilage stresses. J. Biomech. 45, 2149–2156.
Andersen, M.S., Benoit, D.L., Damsgaard, M., Ramsey, D.K., Rasmussen, J., 2010. Do kinematic models reduce the effects of soft tissue artefacts in skin marker-based motion analysis? An in vivo study of knee kinematics. J. Biomech. 43, 268–273.
Anglin, C., Ho, K.C., Briard, J.-L., De Lambilly, C., Plaskos, C., Nodwell, E., Stindel, E., 2008. In vivo patellar kinematics during total knee arthroplasty. Comp. Aid. Surg. 13, 377–391.
Arnold, A.S., Salinas, S., Hakawa, D.J., Delp, S.L., 2000. Accuracy of muscle moment arms estimated from MRI-based musculoskeletal models of the lower extremity. Comput. Aided Surgery 5, 108–119.
Baxter, M.P., 1988. Assessment of normal pediatric knee ligament laxity using the genucom. J. Pediat. Orthoped. 8, 546–550.
Begon, M., Andersen, M.S., Dumas, R., 2018. Multibody kinematics optimization for the estimation of upper and lower limb human joint kinematics: a systematized methodological review. J. Biomech. Eng. 140, 030801.
Belvedere, C., Catani, F., Ensini, A., de la Barrera, J.M., Leardini, A., 2007. Patellar tracking during total knee arthroplasty: an in vitro feasibility study. Knee Surger, Sports Traumatol., Arthrosc. 15, 985–993.
Belvedere, C., Ensini, A., Feliciangeli, A., Cenni, F., D'Angeli, V., Giannini, S., Leardini, A., 2012. Geometrical changes of knee ligaments and patellar tendon during passive flexion. J. Biomech. 45, 1886–1892.
Benoit, D.L., Ramsey, D.K., Lamontagne, M., Xu, L., Wretenberg, P., Renström, P., 2006. Effect of skin movement artifact on knee kinematics during gait and cutting motions measured in vivo. Gait Posture 24, 152–164.

Bergamini, E., Pillet, H., Hausselle, J., Thoreux, P., Guerard, S., Camomilla, V., Cappozzo, A., Skalli, W., 2011. Tibio-femoral joint constraints for bone pose estimation during movement using multi-body optimization. Gait Posture 33, 706–711.
Besl, P.J., McKay, N.D., 1992. A method for registration of 3-D shapes. IEEE Trans. Pattern Anal. Mach. Intellig. 14, 239–256.
Blankevoort, L., Huiskes, R., De Lange, A., 1991. Recruitment of knee joint ligaments. J. Biomech. Eng. 113, 94–103.
Bonci, T., Camomilla, V., Dumas, R., Chèze, L., Cappozzo, A., 2014. A soft tissue artefact model driven by proximal and distal joint kinematics. J. Biomech. 47, 2354–2361.
Brito da Luz, S., Modenese, L., Sancisi, N., Mills, P.M., Kennedy, B., Beck, B.R., Lloyd, D. G., 2017. Feasibility of using MRIs to create subject-specific parallel-mechanism joint models. J. Biomech. 53, 45–55.
Cappozzo, A., Catani, F., Della Croce, U., Leardini, A., 1995. Position and orientation in space of bones during movement: anatomical frame definition and determination. Clin. Biomech. 10, 171–178.
Clément, J., Dumas, R., Hagemeister, N., De Guise, J.A., 2015. Soft tissue artifact compensation in knee kinematics by multi-body optimization: performance of subject-specific knee joint models. J. Biomech. 48, 3796–3802.
Coello, C.A.C., Pulido, G.T., Lechuga, M.S., 2004. Handling multiple objectives with particle swarm optimization. IEEE Trans. Evol. Comput. 8, 256–279.
Dhaher, Y.Y., Kwon, T.-H., Barry, M., 2010. The effect of connective tissue material uncertainties on knee joint mechanics under isolated loading conditions. J. Biomech. 43, 3118–3125.
Feikes, J., O'Connor, J., Zavatsky, A., 2003. A constraint-based approach to modelling the mobility of the human knee joint. J. Biomech. 36, 125–129.
Flynn, J.M., Mackenzie, W., Kolstad, K., Sandifer, E., Jawad, A.F., Galinat, B., 2000. Objective evaluation of knee laxity in children. J. Pediat. Orthopaed. 20, 259–263.
Gasparutto, X., Dumas, R., Jacquelin, E., 2012. Multi-body optimisation with deformable ligament constraints: influence of ligament geometry. Comput. Meth. Biomech. Biomed. Eng. 15, 191–193.
Gasparutto, X., Sancisi, N., Jacquelin, E., Parenti-Castelli, V., Dumas, R., 2015. Validation of a multi-body optimization with knee kinematic models including ligament constraints. J. Biomech. 48, 1141–1146.
Halonen, K., Dzialo, C.M., Mannisi, M., Venäläinen, M., de Zee, M., Andersen, M.S., 2017. Workflow assessing the effect of gait alterations on stresses in the medial tibial cartilage-combined musculoskeletal modelling and finite element analysis. Sci. Rep. 7, 17396.
Hinton, R.Y., Rivera, V.R., Pautz, M.J., Sponseller, P.D., 2008. Ligamentous laxity of the knee during childhood and adolescence. J. Pediat. Orthopaed. 28, 184–187.
Kiapour, A., Kiapour, A.M., Kaul, V., Quatman, C.E., Wordeman, S.C., Hewett, T.E., Demetropoulos, C.K., Goel, V.K., 2014. Finite element model of the knee for investigation of injury mechanisms: development and validation. J. Biomech. Eng. 136, 011002.
Leardini, A., Sawacha, Z., Paolini, G., Ingrosso, S., Nativo, R., Benedetti, M.G., 2007. A new anatomically based protocol for gait analysis in children. Gait Post. 26, 560–571.
Lu, T.-W., Tsai, T.-Y., Kuo, M.-Y., Hsu, H.-C., Chen, H.-L., 2008. In vivo three-dimensional kinematics of the normal knee during active extension under unloaded and loaded conditions using single-plane fluoroscopy. Med. Eng. Phys. 30, 1004–1012.
Macri, E.M., Crossley, K.M., d'Entremont, A.G., Hart, H.F., Forster, B.B., Wilson, D.R., Ratzlaff, C.R., Walsh, A.M., Khan, K.M., 2018. Patellofemoral and tibiofemoral alignment in a fully weight-bearing upright MR: Implementation and repeatability. J. Magnet. Reson. Imaging 47, 841–847.
Marra, M.A., Vanheule, V., Fluit, R., Koopman, B.H., Rasmussen, J., Verdonschot, N., Andersen, M.S., 2015. A subject-specific musculoskeletal modeling framework to predict in vivo mechanics of total knee arthroplasty. J. Biomech. Eng. 137, 020904.
Moissenet, F., Chèze, L., Dumas, R., 2014. A 3D lower limb musculoskeletal model for simultaneous estimation of musculo-tendon, joint contact, ligament and bone forces during gait. J. Biomech. 47, 50–58.
Mootanah, R., Imhauser, C., Reisse, F., Carpanen, D., Walker, R., Koff, M., Lenhoff, M., Rozbruch, S., Fragomen, A., Dewan, Z., 2014. Development and validation of a computational model of the knee joint for the evaluation of surgical treatments for osteoarthritis. Comput. Meth. Biomech. Biomed. Eng. 17, 1502–1517.
Navacchia, A., Kefala, V., Shelburne, K.B., 2017. Dependence of muscle moment arms on in vivo three-dimensional kinematics of the knee. Ann. Biomed. Eng. 45, 789–798.
Ottoboni, A., Parenti-Castelli, V., Sancisi, N., Belvedere, C., Leardini, A., 2010. Articular surface approximation in equivalent spatial parallel mechanism models of the human knee joint: an experiment-based assessment. Proc. Inst. Mech. Eng., Part H: J. Eng. Med. 224, 1121–1132.
Parenti-Castelli, V., Di Gregorio, R., 2000. Parallel mechanisms applied to the human knee passive motion simulation, Advances in Robot Kinematics. Springer, pp. 333–344.
Pataky, T.C., Robinson, M.A., Vanrenterghem, J., 2013. Vector field statistical analysis of kinematic and force trajectories. J. Biomech. 46, 2394–2401.
Pataky, T.C., Vanrenterghem, J., Robinson, M.A., 2015. Zero-vs. one-dimensional, parametric vs. non-parametric, and confidence interval vs. hypothesis testing procedures in one-dimensional biomechanical trajectory analysis. J. Biomech. 48, 1277–1285.
Penny, W.D., Friston, K.J., Ashburner, J.T., Kiebel, S.J., Nichols, T.E., 2011. Statistical Parametric Mapping: The Analysis of Functional Brain Images. Elsevier.
Reinschmidt, C., van den Bogert, A.J., Nigg, B.M., Lundberg, A., Murphy, N., 1997. Effect of skin movement on the analysis of skeletal knee joint motion during running. J. Biomech. 30, 729–732.
Sancisi, N., Gasparutto, X., Parenti-Castelli, V., Dumas, R., 2017. A multi-body optimization framework with a knee kinematic model including articular contacts and ligaments. Meccanica 52, 695–711.
Sancisi, N., Parenti-Castelli, V., 2011a. A new kinematic model of the passive motion of the knee inclusive of the patella. J. Mech. Robot. 3, 041003.
Sancisi, N., Parenti-Castelli, V., 2011b. A novel 3d parallel mechanism for the passive motion simulation of the patella-femur-tibia complex. Meccanica 46, 207–220.
Stagni, R., Fantozzi, S., Cappello, A., 2009. Double calibration vs. global optimisation: performance and effectiveness for clinical application. Gait Posture 29, 119–122.
Wilson, D., Feikes, J., O'connor, J., 1998. Ligaments and articular contact guide passive knee flexion. J. Biomech. 31, 1127–1136.
Wilson, D., O'Connor, J., 1997. A three-dimensional geometric model of the knee for the study of joint forces in gait. Gait Posture 5, 108–115.